

Fast Approximate Quantification of Endovascular Stent Graft Displacement Forces in the Bovine Aortic Arch Variant

Journal of Endovascular Therapy

1–13

© The Author(s) 2022





Article reuse guidelines:

sagepub.com/journals-permissions

DOI: 10.1177/15266028221095403

www.jevt.org



Francesco Sturla, PhD^{1,2} , Alessandro Caimi, PhD²,
 Rodrigo M. Romarowski, PhD¹, Giovanni Nano, MD^{3,4},
 Mattia Glauber, MD⁵, Alberto Redaelli, PhD², Emiliano Votta, PhD^{2,1},
 and Massimiliano M. Marrocco-Trischitta, MD, PhD^{3,6} 

Abstract

Purpose: Displacement forces (*DFs*) identify hostile landing zones for stent graft deployment in thoracic endovascular aortic repair (TEVAR). However, their use in TEVAR planning is hampered by the need for time-expensive computational fluid dynamics (CFD). We propose a novel fast-approximate computation of *DFs* merely exploiting aortic arch anatomy, as derived from the computed tomography (CT) and a measure of central aortic pressure. **Materials and Methods:** We tested the fast-approximate approach against CFD gold-standard in 34 subjects with the “bovine” aortic arch variant. For each dataset, a 3-dimensional (3D) model of the aortic arch lumen was reconstructed from computed tomography angiography and CFD then employed to compute *DFs* within the aortic proximal landing zones. To quantify fast-approximate *DFs*, the wall shear stress contribution to the *DF* was neglected and blood pressure space-distribution was averaged on the entire aortic wall to reliably approximate the patient-specific central blood pressure. Also, *DF* values were normalized on the corresponding proximal landing zone area to obtain the equivalent surface traction (*EST*). **Results:** Fast-approximate approach consistently reflected ($r^2=0.99$, $p<0.0001$) the *DF* pattern obtained by CFD, with a -1.1% and 0.7° bias in *DFs* magnitude and orientation, respectively. The normalized *EST* progressively increased ($p<0.0001$) from zone 0 to zone 3 regardless of the type of arch, with proximal landing zone 3 showing significantly greater forces than zone 2 ($p<0.0001$). Upon *DF* normalization to the corresponding aortic surface, fast-approximate *EST* was decoupled in blood pressure and a dimensionless shape vector (*S*) reflecting aortic arch morphology. *S* showed a zone-specific pattern of orientation and proved a valid biomechanical blueprint of *DF* impact on the thoracic aortic wall. **Conclusion:** Requiring only a few seconds and quantifying clinically relevant biomechanical parameters of proximal landing zones for arch TEVAR, our method suits the real preoperative decision-making process. It paves the way toward analyzing large population of patients and hence to define threshold values for a future patient-specific preoperative TEVAR planning.

Keywords

thoracic aorta endovascular repair, computational fluid dynamics, displacement forces, endovascular planning, bovine aortic arch variant

Introduction

Thoracic endovascular aortic repair (TEVAR) is a well-established therapeutic option in patients with adequate anatomic features¹ and an acceptable life expectancy.² Yet, while TEVAR of the descending thoracic aorta currently represents a first-line treatment,³ TEVAR of the aortic arch is associated with relevant rates of postoperative clinical failure,⁴ and still poses specific challenges related to the peculiar geometric configuration and unique fluid dynamic environment⁵ of this aortic tract.

Current preoperative planning of TEVAR remains based on computed tomography angiography (CTA) imaging protocols,

which disregard the fact that the aorta is a pressurized conduit subjected to displacement forces (*DFs*).⁶ Magnitude and orientation of *DFs* identify landing zones with a hostile biomechanical environment,⁷ which are associated with dismal proximal endograft performance after its intraluminal deployment.⁸

Despite the awareness of this limitation, however, the inclusion of *DF* evaluation into TEVAR planning continues to be hampered by the time-expense required by the only approach proposed so far to quantify *DFs*, ie, computational fluid dynamics (CFD), which yields the spatial distribution of blood pressure and wall shear stress (τ) acting

on the aortic wall and determining DF_s .^{5,6,9–11} Furthermore, such time-expense prevents from analyzing DF_s in a statistically meaningful population of TEVAR candidates, which is the mandatory preliminary step to identify reliable clinically relevant threshold values for the extracted parameters.¹²

In the present work, to overcome the need of time-consuming CFD analyses, we sought to develop a fast approximate and reliable approach to compute DF_s in the aortic arch. Our approach relied on previous observations from studies on the biomechanical modeling of the aortic arch,^{5,7,8} which suggested that blood pressure is the primary contributor to the DF magnitude, while τ impact only accounts for less than 1% of the overall DF magnitude,^{5,13} and the orientation of DF_s largely depends on the aortic anatomic features.^{5,6,11}

Furthermore, aortic blood pressure is reported to be only slightly heterogeneous along the aortic arch.^{14–16} Accordingly, we herein hypothesized that blood pressure space distribution within the aortic arch can be reasonably simplified with a single clinically pertinent value of pressure, eg, a noninvasive measure of the central aortic pressure. Based on this evidence, we hypothesized that DF_s could be quantified on a patient-specific basis with negligible approximation merely on the basis of aortic 3D anatomy as reconstructed from CT-scans and central aortic pressure, thus bypassing burdensome CFD analysis.

To test the validity of the proposed fast approximate approach against CFD reference analysis, we chose to prove our case in subjects ($n=30$) presenting with the so called “bovine” aortic arch,¹⁷ which is the second most common anatomic variant after the standard arch configuration, and is characterized by a common origin of the innominate and left carotid artery (CILCA arch).¹⁸ Notably, this anatomic pattern is highly prevalent among patients requiring TEVAR,¹⁹ being a recognized risk factor for the development of thoracic aortic disease,²⁰ and it presents a consistent and peculiar geometric pattern.¹⁹

Materials and Methods

Study Design

The newly introduced fast approximate approach was tested on 30 anonymized thoracic CTA scans of subjects with a

CILCA arch configuration and a healthy aorta. In addition to this group, 4 more cases of patients with a CILCA arch and an aneurysmatic aorta, which were retrieved from a database of patients treated by TEVAR at our center, were also included. On these CTAs, both the new fast approximate approach and CFD analyses were performed to (1) confirm that in CILCAs the pattern of DF resembles that observed in standard arches, consistently with previous findings,⁷ and (2) to test the fast-approximate method in a more challenging TEVAR planning scenario.

The CTAs of 30 healthy aortas all respected the following criteria: thin-cut (1.0 mm), visible origins of the supra-aortic branches, patient age >60 years, thoracic aorta diameter <40 mm, arch radius of curvature >20 mm, no previous aortic surgery, and no radiologic signs of aortic pathology, including dissection, intramural hematoma, or penetrating aortic ulcer. CTAs were evenly selected among 3 anatomical phenotypes, ie, arch types I, II, and III,²¹ based on the vertical distance from the origin of the brachiocephalic trunk to the top of the arch²²: this distance is shorter than the left common carotid artery diameter (D_{CCA}) in arch type I, in the range $D_{CCA} \div 2 \cdot D_{CCA}$ in arch type II, and longer than $2 \cdot D_{CCA}$ in a type III arch (Figure 1). In addition, 4 CTAs from patients with CILCA arch configuration and aortic aneurysm, respectively, with proximal landing zone 2 (cases A02, A09 and A10) or 3 (case A01), were included in the study as term of comparison and to preliminarily confirm initial proof-of-concept findings in diseased aortas.

The study was approved by the Ethics Committee of reference; informed consent was waived by the Ethics Committee because of the retrospective nature of the study and the analysis of anonymized images. The study was conducted according to the principles outlined in the Declaration of Helsinki.

Aortic reconstruction

Each CTA scan was segmented in Mimics Medical v21.0 (Materialise, Leuven) to reconstruct the thoracic aorta, from the aortic valve annulus to the diaphragm, and including the proximal tract of the innominate artery, the left common carotid artery, and the left subclavian artery (Figure 2a).

¹3D and Computer Simulation Laboratory, IRCCS Policlinico San Donato, San Donato Milanese, Italy

²Department of Electronics Information and Bioengineering, Politecnico di Milano, Milano, Italy

³Vascular Surgery Unit, Cardiovascular Department, IRCCS Policlinico San Donato, San Donato Milanese, Italy

⁴Dipartimento di Scienze Biomediche per la Salute, Università degli Studi di Milano, Milano, Italy

⁵Minimally Invasive Cardiac Surgery Unit, Istituto Clinico Sant’Ambrogio, Milano, Italy

⁶Clinical Research Unit, Cardiovascular Department, IRCCS Policlinico San Donato, San Donato Milanese, Italy

Corresponding Author:

Francesco Sturla, 3D and Computer Simulation Laboratory, IRCCS Policlinico San Donato, Via Morandi 30, San Donato Milanese, Milano, Italy.

Email: francesco.sturla@grupposandonato.it

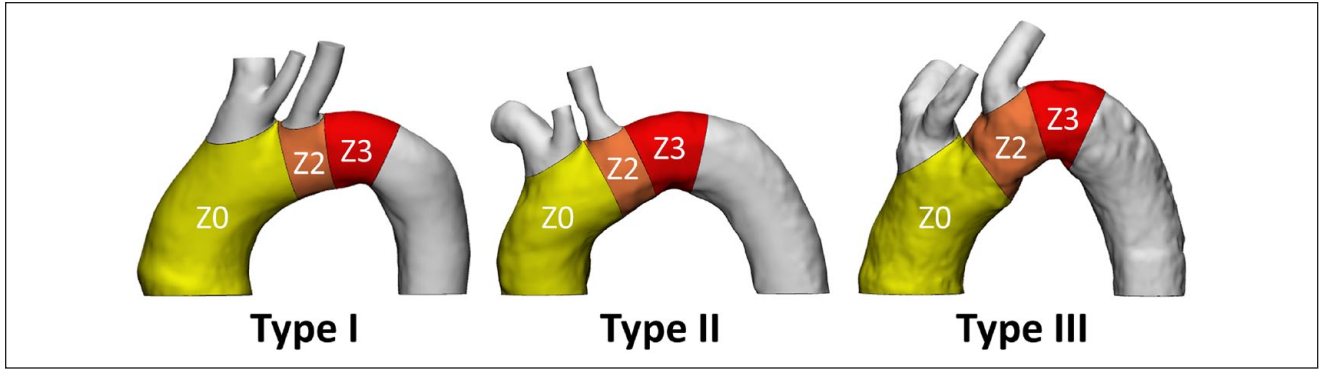


Figure 1. Aortic arch classification. Aortic arch classification in types I, II, and III and subdivision in the Ishimaru's zones, ie, zones 0 (Z0), 2 (Z2) and 3 (Z3).

Subsequently, each 3D aortic geometry was imported in stereolithographic format (.stl) in the open-source library Vascular Modelling ToolKit (VMTK v1.4; www.vmtk.org). Straight flow extensions were added at both the inlet and the outlet faces of the domain to ensure a fully developed velocity profile at the inlet section and to minimize the influence of outlet boundary conditions.^{23,24} These fictitious extensions were not part of the aortic domain of interest for postprocessing analysis.

The final 3D model was then discretized to generate a volumetric grid suitable for CFD analysis within the aorta²⁵; an average cut-off of 2 million tetrahedral cells was considered for all the simulated anatomies, following a preliminary mesh convergence analysis.⁵ The triangular faces of the cells that belonged to the aortic wall were tagged for subsequent processing.

CFD Analysis

Numerical simulations (Figure 2b) were carried out, by solving the unsteady Navier-Stokes equations in the region of interest through the open-source finite element solver LifeV (www.lifev.org) following a previously employed and well-established CFD approach.^{5,7,26} To obtain periodic pulsatile flow conditions, 6 consecutive heartbeats with a 1 s period were simulated in unsteady conditions with a constant time step of 0.001 s. CFD data computed in the last cardiac cycle were postprocessed.

Blood was treated as a Newtonian fluid with constant viscosity ($\mu=3.5$ cP) and density ($\rho=1060$ kg/m³); aortic wall was assumed rigid and no-slip (ie, null velocity) boundary conditions were prescribed on the luminal surface.

Given the retrospective nature of the study, patient-specific hemodynamic data were not available, and the same inflow and outflow boundary conditions were applied in all cases.⁵ Specifically, on the inflow section, a pulsatile aortic flow waveform with a cardiac output of 4.88 L/min was

imposed as representative of ascending aortic flow waveform and cardiac output for adult patients. This flow waveform, derived from phase contrast magnetic resonance imaging on a previous cohort of patients investigated at our study hospital, was extracted as the mean flow waveform measured at the level of the ascending aorta. At each outflow section, a 3-element Windkessel circuit was coupled to the 3D discretized domain to reliably mimic both compliance and resistance of the distal aortic vasculature,²⁶ thus resulting in a physiological range of the average simulated blood pressure.²⁷

CFD Postprocessing

CFD results were postprocessed at peak systole in Paraview v5.5.2 (Kitware Inc, Clifton Park, NY), using dedicated Python scripts to quantify 3D displacement forces (\mathbf{DF}) acting on the aortic arch wall according to the approach proposed by Figueroa et al.⁶ To this purpose, both blood flow pressure (p) and wall shear stress ($\boldsymbol{\tau}$) distributions on the aortic wall were extracted (Figure 2c).

Displacement forces - The displacement force \mathbf{DF}_{CFD} , expressed in N, was calculated at peak systole on each Ishimaru's proximal landing zone (ie, $A=Z0, Z2$, and $Z3$, Figure 2d), as defined according to the Modified Arch Landing Areas Nomenclature (Figure 1).^{19,21} The following formula was used²⁸:

$$\mathbf{DF}_{CFD} = \sum_{i=1}^{N_{cell}} p_i \mathbf{n}_i A_i + \sum_{i=1}^{N_{cell}} \boldsymbol{\tau}_i A_i \quad (1)$$

where N_{cell} is the number of triangular faces belonging to the landing zone, A_i and \mathbf{n}_i are the extent and the outward normal unit vector of the i th triangular face, p_i and $\boldsymbol{\tau}_i$ are the pressure and the wall shear stress vector acting on it. Each force vector is applied in the center of mass of the wall surface of the relevant landing zone.

Equivalent surface traction (\mathbf{EST}_{CFD}) - As the surface areas of the proximal landing zones are different across the

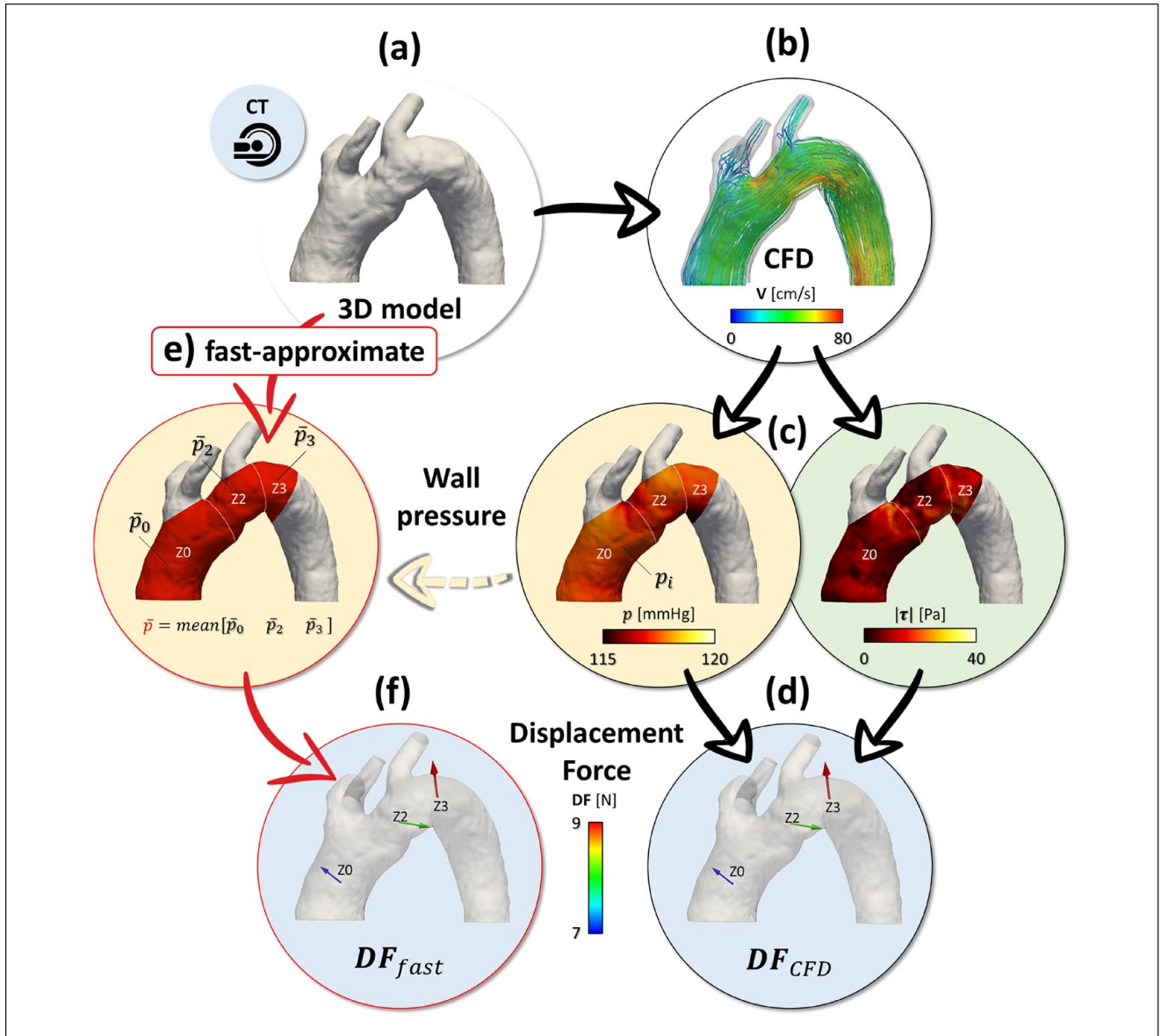


Figure 2. Study workflow and displacement forces computation. Patient-specific 3D geometry (a) used to simulate pulsatile aortic blood flow through CFD analysis (b); blood pressure and shearing stresses acting on the aortic wall surface (c) were extracted to compute displacement forces (d). Assuming a mean blood pressure acting on the aortic wall (e), we defined a novel fast-approximate quantification of aortic displacement forces (f). CFD, computational fluid dynamics; CT, computed tomography; DF, displacement force.

arch, each DF_{CFD} was normalized by the surface area (A) of the corresponding proximal landing zone area⁵:

$$EST_{CFD} = \frac{DF_{CFD}}{A} = \frac{\sum_{i=1}^{N_{cell}} p_i n_i A_i + \sum_{i=1}^{N_{cell}} \tau_i A_i}{\sum_{i=1}^{N_{cell}} A_i} \quad (2)$$

where EST_{CFD} magnitude is expressed in N m^{-2} .

Fast-Approximate DF Quantification

Fast-approximate DF (DF_{fast}) was quantified based on the following 2 assumptions (Figure 2).

First, we neglected the wall shear stress contribution to DF since blood pressure has already been demonstrated to be several orders of magnitude larger than the corresponding τ contribution,⁶ thus resulting the dominant contributor to the overall DF .¹¹

Second, the CFD-derived blood pressure distribution acting on the aortic wall surface was approximated. To this purpose, blood pressure distribution was averaged within each aortic landing zone as \bar{p}_j :

$$\bar{p}_j = \frac{\sum_{i=1}^{N_{cell}} p_i}{N_{cell}} \quad (3)$$

with $j=0, 2$, and 3 , respectively. Subsequently, aortic mean blood pressure \bar{p} was averaged between \bar{p}_0 , \bar{p}_2 , and \bar{p}_3 , and rounded to the closest integer pressure value in clinical units of millimeters of mercury (mmHg), to represent a reliable surrogate of the patient-specific central systolic blood pressure (Figure 2e, Supplementary Tables 1 and 2). Accordingly, \mathbf{DF}_{fast} was quantified as:

$$\mathbf{DF}_{fast} = \bar{p} \sum_{i=1}^{N_{cell}} \mathbf{n}_i A_i \quad (4)$$

pulling \bar{p} out of the summation as a constant (Figure 2f). Each \mathbf{DF}_{fast} vector was compared with the corresponding \mathbf{DF}_{CFD} one in terms of their magnitude; in addition, the angle δ between the 2 vectors was computed as a measure of their collinearity.

Subsequently, \mathbf{DF}_{fast} values were normalized on the corresponding proximal landing zone area to obtain \mathbf{EST}_{fast} :

$$\mathbf{EST}_{fast} = \frac{\mathbf{DF}_{fast}}{A} = \bar{p} \frac{\sum_{i=1}^{N_{cell}} \mathbf{n}_i A_i}{\sum_{i=1}^{N_{cell}} A_i} = \bar{p} \mathbf{S} \quad (5)$$

where \mathbf{EST}_{fast} quantification was decoupled in the product between a pressure factor (\bar{p}), whose units are N m^{-2} , and a dimensionless shape vector \mathbf{S} , which is only dependent on the 3D aortic surface morphology. The direction cosines (α , β , γ) of \mathbf{S} were then calculated as:

$$\begin{aligned} \alpha &= \cos^{-1} \left(\frac{S_x}{|\mathbf{S}|} \right) \\ \beta &= \cos^{-1} \left(\frac{S_y}{|\mathbf{S}|} \right) \\ \gamma &= \cos^{-1} \left(\frac{S_z}{|\mathbf{S}|} \right) \end{aligned} \quad (6)$$

$|\mathbf{S}|$ is the magnitude of \mathbf{S} , and S_x , S_y , S_z are the components of \mathbf{S} along 3 anatomical and mutually orthogonal directions: right-left (x), antero-posterior (y) and superior-inferior (z). Angles α , β , γ indicate the inclination of \mathbf{S} with respect to them.

Statistical Analysis

Continuous variables were expressed as mean \pm standard deviation (SD) after Shapiro-Wilk normality tests. $|\mathbf{DF}|$ and $|\mathbf{EST}|$ were compared using 2-way analysis of variance and considering both arch type and landing zone as independent factors; Bonferroni correction was used in post hoc analysis. Pairwise comparison between fast-approximate and CFD results was accomplished within each

landing zone using a paired t test; differences were assessed through Bland-Altman plots and correlations were analyzed with linear regression. Statistical analyses were performed using GraphPad Prism 7 (GraphPad Software Inc, La Jolla, CA); a p value lower than 0.05 was considered significant.

Results

\mathbf{DF}_{fast} and \mathbf{EST}_{fast} , quantified within each Ishimaru's proximal landing zone,¹⁹ were compared against the corresponding \mathbf{DF}_{CFD} and \mathbf{EST}_{CFD} vector, respectively.

Magnitude of \mathbf{DF}_{fast} and \mathbf{EST}_{fast}

The magnitude of fast-approximate displacement forces, ie, $|\mathbf{DF}_{fast}|$, significantly differed ($p < 0.0001$) between the aortic landing zones, reporting the highest values in zone 0 (Figure 3a, Supplementary Table 3). Given the remarkable extent of zone 0, such a behavior resulted from the combination of \mathbf{DF} s between the inner and the outer aortic curvature. $|\mathbf{DF}_{fast}|$ showed no differences in relation to the arch type ($p = 0.92$).

The normalized forces $|\mathbf{EST}_{fast}|$ progressively increased ($p < 0.0001$) from zone 0 to zone 3 within each type of arch (Figure 3b, Supplementary Table 4). Of note, zone 3 showed a significantly greater $|\mathbf{EST}_{fast}|$ than zone 2 ($p < 0.0001$), which entails being a biomechanically hostile landing zone for TEVAR. Indeed, $|\mathbf{EST}_{fast}|$ values ranged between 966 and 3741 N m^{-2} in zone 2, and between 1437 and 5907 N m^{-2} in zone 3 (Supplementary Table 2).

Differences remained negligible within each landing zone when comparing $|\mathbf{EST}_{fast}|$ between the types of arch ($p = 0.41$).

Additional data extracted from the 4 anatomies with aneurysmatic CILCA arch (Supplementary Tables 5 and 6) provided $|\mathbf{EST}_{fast}|$ values comparable with the ones collected in the healthy aortic anatomies, consistently with previous findings.⁷ Zone 3 was characterized by $|\mathbf{EST}_{fast}|$ values in the range $3994 \div 5816 \text{ N m}^{-2}$, ie, at least 2-fold as compared with those computed in zone 2 (range $863 \div 2339 \text{ N m}^{-2}$, Supplementary Table 6).

Orientation of \mathbf{DF}_{fast} and \mathbf{EST}_{fast} : The Aortic Shape Vector

The present fast-approximate approach allowed to represent the spatial orientation of aortic displacement forces, being the same for both \mathbf{DF}_{fast} and \mathbf{EST}_{fast} , using the dimensionless aortic shape vector \mathbf{S} (Supplementary Tables 7 and 8) from equation (5), and its inclination, ie, α , β , γ as in equation (6) with respect to the anatomical directions. We assessed (\mathbf{S}) within each aortic landing zone for each healthy anatomy (Figure 4a). Despite the inter-subject anatomical variability, a repeatable zone-specific pattern of \mathbf{S}

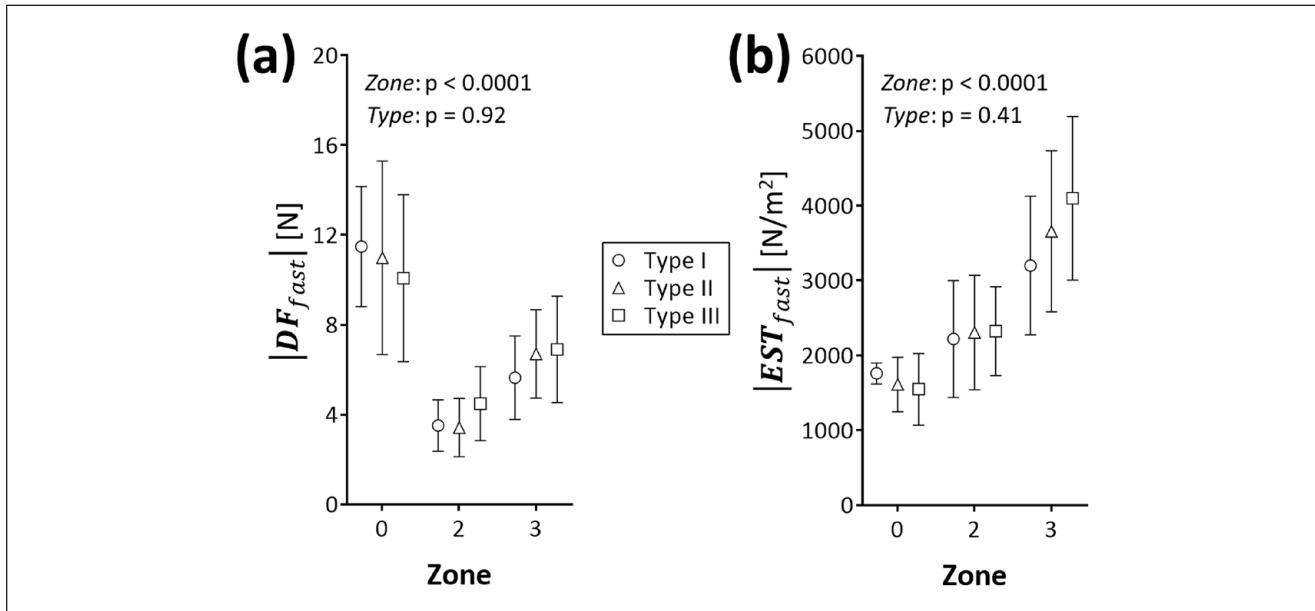


Figure 3. Fast-approximate magnitude quantification of displacement force $|\mathbf{DF}_{fast}|$ (a) and equivalent surface traction $|\mathbf{EST}_{fast}|$ (b), distinguishing between arch type and zones, in the healthy CILCA subjects.

orientations was obtained (Figure 4b, Supplementary Table 9): in zone 0, it was oriented in the right ($\alpha > 90^\circ$), anterior-superior ($\beta > 90^\circ$ and $\gamma < 90^\circ$) direction; in zone 2, it was skewed on the left ($\alpha < 90^\circ$) and oriented in the posterior-inferior ($\beta < 90^\circ$ and $\gamma > 90^\circ$) direction; in zone 3, the superior direction dominated ($\gamma < 90^\circ$).

In the pathological aortic anatomies (Figure 4c, Supplementary Table 10), though \mathbf{S} magnitude remained comparable with healthy aortic arches, the vector orientation clearly reflected the anatomical alteration induced by the aortic aneurysm. Indeed, in zone 3, the degree of aortic wall dilation progressively exacerbated the anterior \mathbf{S} orientation.

As clear from equation (5), \mathbf{S} depends on the oriented area of the triangles obtained when discretizing the aortic wall. Hence, we evaluated the sensitivity of \mathbf{S} to the grid space-resolution of the aortic surface used to feed the fast-approximate method (Figure 5). Variation of \mathbf{S} in terms of magnitude and direction cosines (α , β , γ) proved to be negligible over a rather broad range of characteristic dimension of the triangulated surfaces that represents the aortic wall surface: from a CFD-usable high-resolution grid (characteristic dimension in the range $200 \div 500 \mu\text{m}$) up to a coarse grid (characteristic dimension of 2mm).

Fast-Approximate Approach vs CFD Gold-Standard Analysis

The fast-approximate quantification of displacement forces consistently reflected the pattern obtained by CFD analysis (Figure 6).

Confirming the results of the fast-approximate approach, differences remained negligible within each landing zone when comparing both $|\mathbf{DF}_{CFD}|$ and $|\mathbf{EST}_{CFD}|$ between the types of arch ($p=0.93$ and $p=0.43$, respectively), with zone 3 reporting the highest $|\mathbf{EST}_{CFD}|$ values, up to 5999 N m^{-2} (Supplementary Table 2).

In Figure 7, pairwise comparison between fast-approximate and CFD computations are reported in terms of $|\mathbf{DF}|$ and $|\mathbf{EST}|$ for all the investigated aortic anatomies.

Specifically, we compared the overall $|\mathbf{DF}|$ percentage differences between fast-approximate method and CFD analysis (Figure 8a): the Bland-Altman plot exhibited a bias of -1.1% and limits of agreement from -5.1% to $+2.8\%$, highlighting that $|\mathbf{DF}_{fast}|$ slightly underestimated $|\mathbf{DF}_{CFD}|$.

The fast-approximate computation strongly correlated against the CFD gold-standard (Figure 8b), ie, $r^2=0.99$ ($p < 0.0001$, slope regression 95% CI of 0.975 to 0.984, $y=0.98x + 0.04$). Of note, these differences were not uniformly distributed between the different aortic landing zones (Figure 8c). Specifically, $|\mathbf{DF}_{fast}|$ underestimated $|\mathbf{DF}_{CFD}|$ in zones 0 and 3 (bias of -2.5% and -1.8% , respectively), but overestimated $|\mathbf{DF}_{CFD}|$ in zone 2 (bias of $+0.9\%$). Nonetheless, within each landing zone, overall limits of agreement of $|\mathbf{DF}|$ differences remained between -4.5% (zone 0) and $+4.4\%$ (zone 2).

Furthermore, CFD analysis (Figure 9, Supplementary Table 11) confirmed that aortic blood pressure (P) was the dominant contributor to the overall $|\mathbf{DF}_{CFD}|$.⁵ Indeed, the contribution due to wall shear stress $|\mathbf{DF}_{CFD,\tau}|$ ranged between 0.2% and 1.6% of $|\mathbf{DF}_{CFD,P}|$. Notably, however, although negligible as compared with $|\mathbf{DF}_{CFD,P}|$, $|\mathbf{DF}_{CFD,\tau}|$

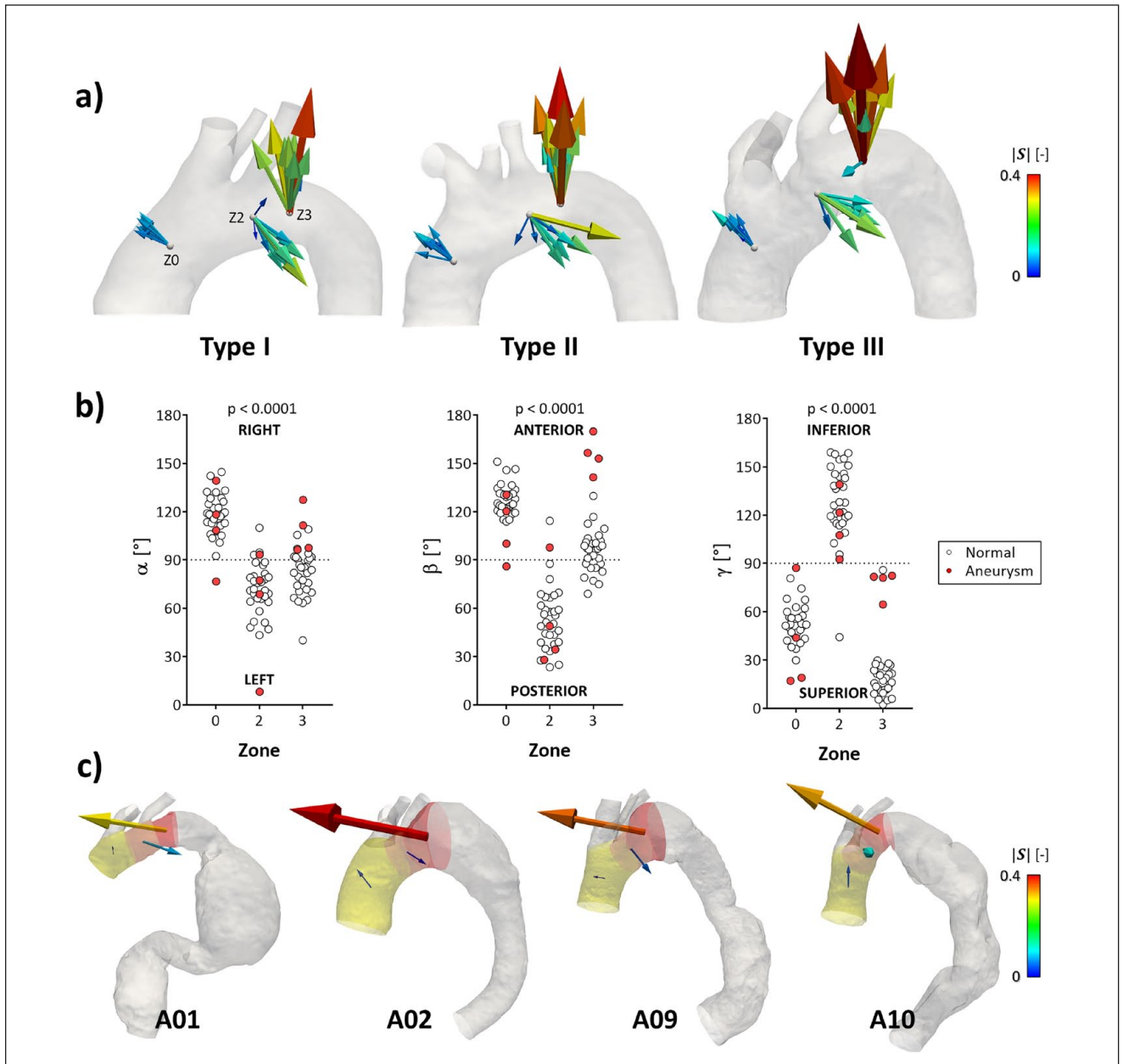


Figure 4. Magnitude and direction of the aortic shape vector S (a) for each analyzed healthy CILCA anatomy within the corresponding arch type subgroup; (b) direction cosines along the left-right (α), anterior-posterior (β) and superior-inferior (γ) anatomical directions computed for each healthy and aneurysmatic (c) anatomy with CILCA arch configuration.

showed the same pattern of differences between the aortic landing zones ($p < 0.0001$). Differences related to the arch type remained not statistically significant for both $|DF_{CFD,P}|$ ($p = 0.94$) and $|DF_{CFD,\tau}|$ ($p = 0.21$).

In the small cohort of anatomies with aneurysmatic CILCA arch, $|EST_{fast}|$ values well agreed with the corresponding $|EST_{CFD}|$ ones, with $|EST_{fast}|$ percentage absolute variations largely below 3% (Supplementary Table 4).

Within each proximal landing zone, we also analyzed the collinearity of each DF_{fast} vector with the corresponding DF_{CFD} one in terms of the angle (δ) between them (Figure 8d,

Supplementary Tables 12 and 13): δ was equal to $0.3^\circ \pm 0.2^\circ$ in zone 0, $1.2^\circ \pm 0.8^\circ$ in zone 2 and $0.7^\circ \pm 0.4^\circ$ in zone 3 ($p < 0.0001$). Consistently, equivalent results were obtained when comparing EST_{fast} against EST_{CFD} .

Discussion

In the present work, we demonstrated that fast-approximate and reliable quantification of displacement forces is feasible in the aortic arch, and this may overcome the need for time-consuming CFD analyses.^{6,11,12}

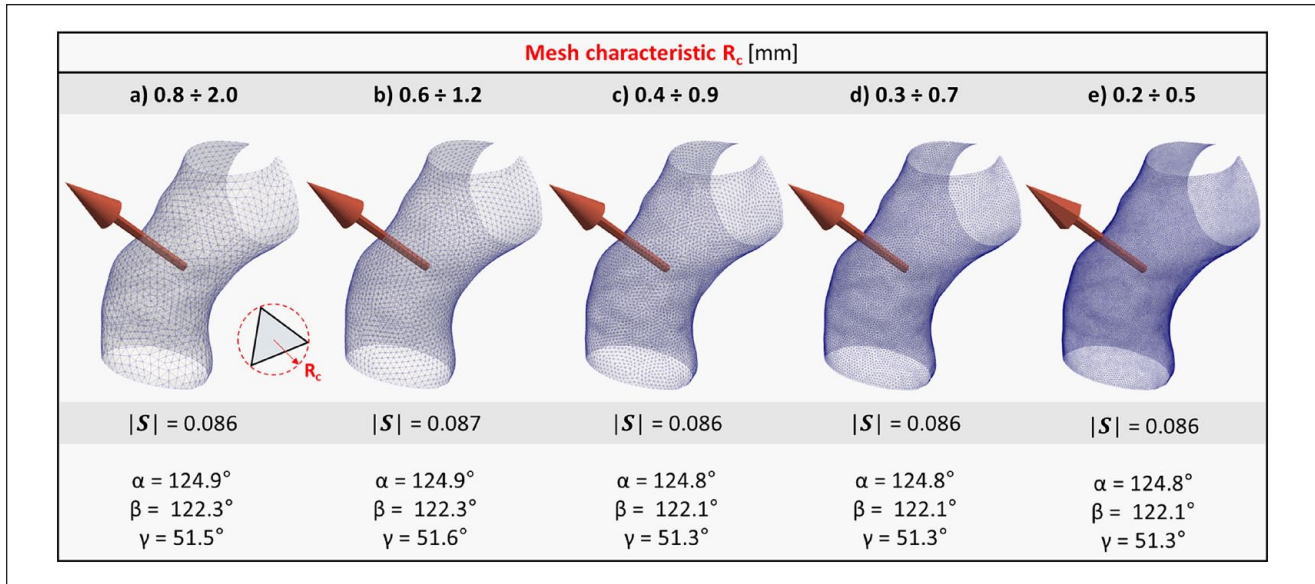


Figure 5. Sensitivity of \mathbf{S} to grid space-resolution: variation of the shape vector \mathbf{S} , in terms of magnitude $|\mathbf{S}|$ and direction cosines (α , β , γ) at different levels of spatial resolution (expressed in terms of the characteristic triangle dimension R_c) of the aortic surface grid employed for the computation of displacement forces according to the fast-approximate method.

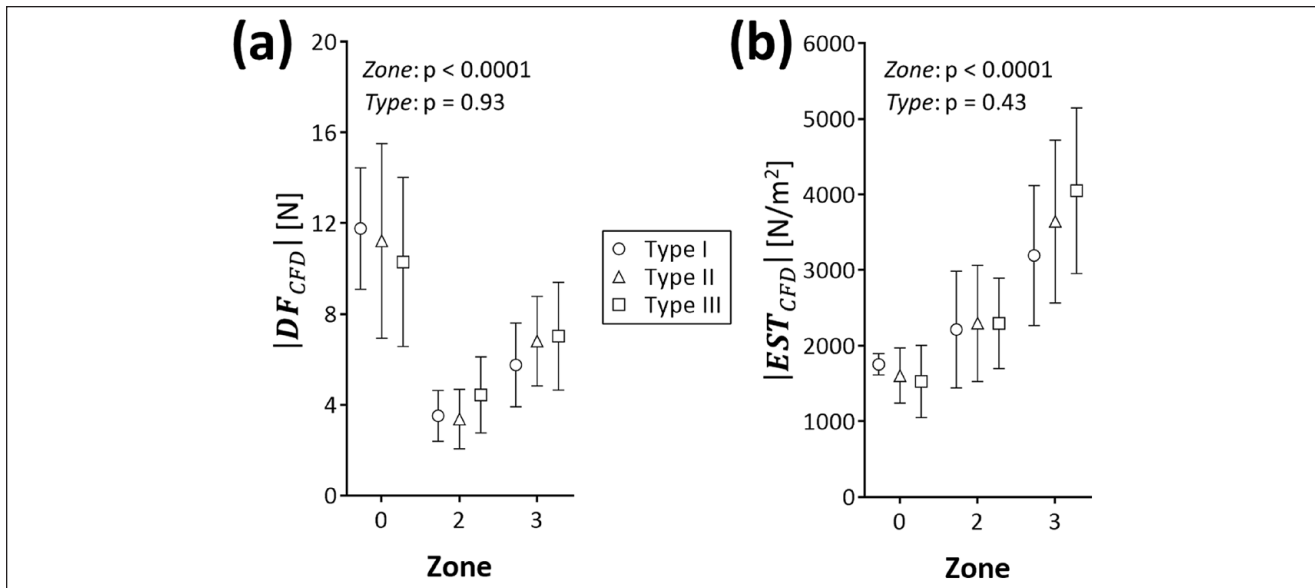


Figure 6. CFD-derived magnitude of (a) displacement force $|\mathbf{DF}_{CFD}|$ and (b) equivalent surface traction $|\mathbf{EST}_{CFD}|$, distinguishing between arch type and zones, in the healthy CILCA subjects. CFD, computational fluid dynamics.

Our fast-approximate approach reproduced accurately enough the \mathbf{DF}_{CFD} vectors extracted from the gold-standard CFD analysis with overall $|\mathbf{DF}_{fast}|$ differences from $|\mathbf{DF}_{CFD}|$ largely below 5%. Within each zone, the orientation of each \mathbf{DF}_{fast} vector well resembled the corresponding one computed from CFD, with small differences in terms of their collinearity represented by the computed δ angle. Hence, comparing the results obtained with the fast-approximate DF evaluation against those provided by the

CFD gold standard, the differences that we obtained did not affect the interpretation of the data of interest.

If compared with time-consuming CFD analysis, which may require several days even exploiting dedicated high-performant computing resources, the computational cost of fast-approximate DF calculation is quantifiable in seconds once the aortic arch geometry is segmented. Hence, the computation of \mathbf{DF}_{fast} and \mathbf{EST}_{fast} is compatible with the timing of TEVAR preoperative planning.

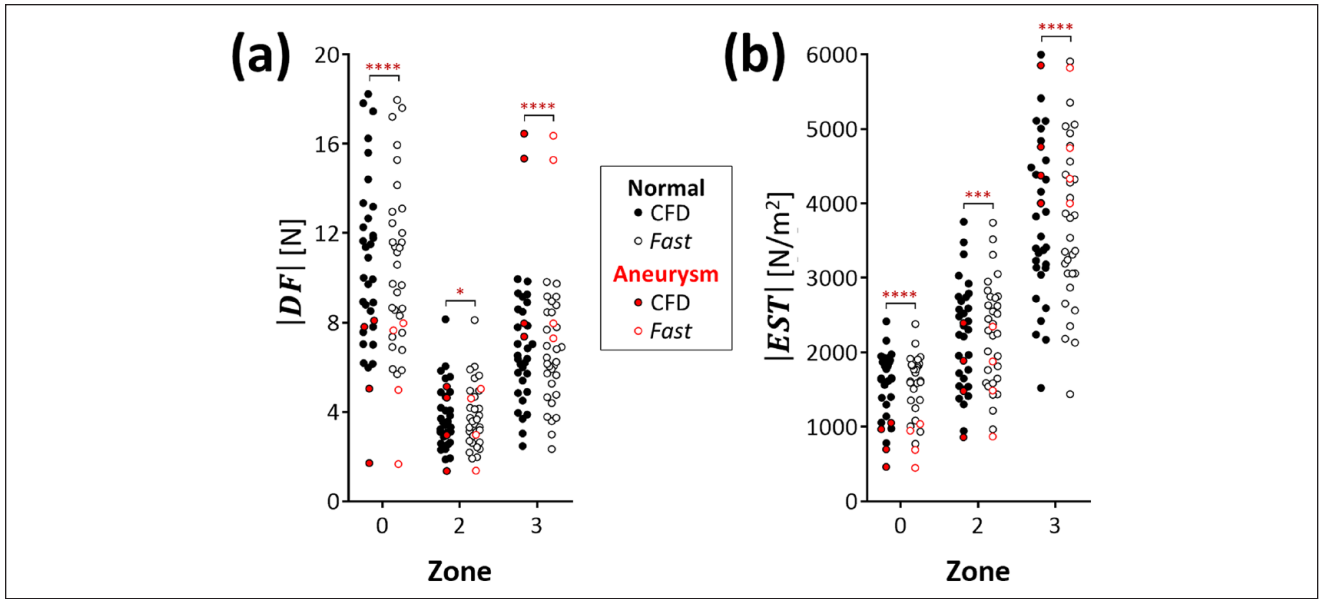


Figure 7. Pairwise comparison in terms of (a) $|DF|$ and (b) $|EST|$ results between fast-approximate approach and CFD gold-standard techniques, in all the simulated aortic anatomies. CFD, computational fluid dynamics; DF, displacement force; EST, equivalent surface traction.

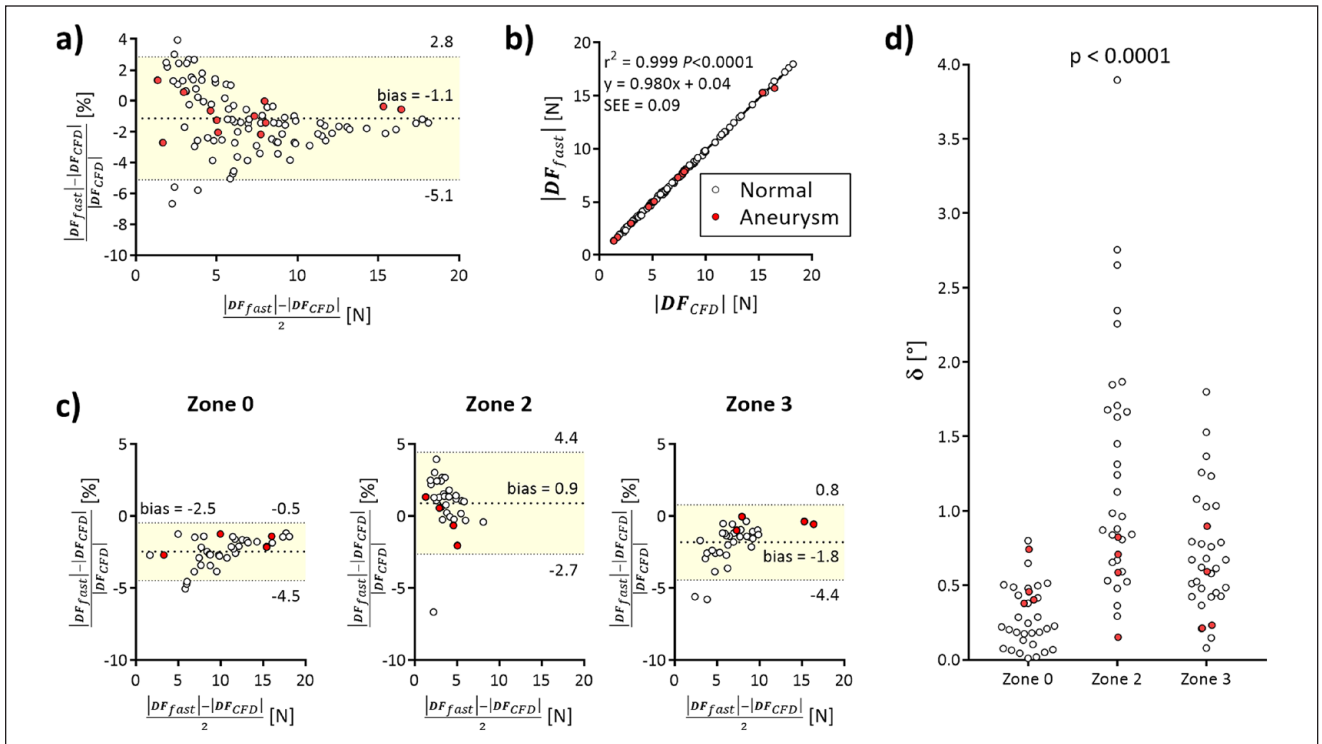


Figure 8. Bland-Altman plot (a) of the differences between $|DF_{fast}|$ and $|DF_{CFD}|$ gold-standard; (b) $|DF|$ correlation between fast-approximate and CFD methods; (c) Bland-Altman plots of percentage $|DF|$ differences within each landing zone; (d) angle (δ) between the same DF vector computed according to fast-approximate approach and CFD analysis, respectively. CFD, computational fluid dynamics; DF, displacement force.

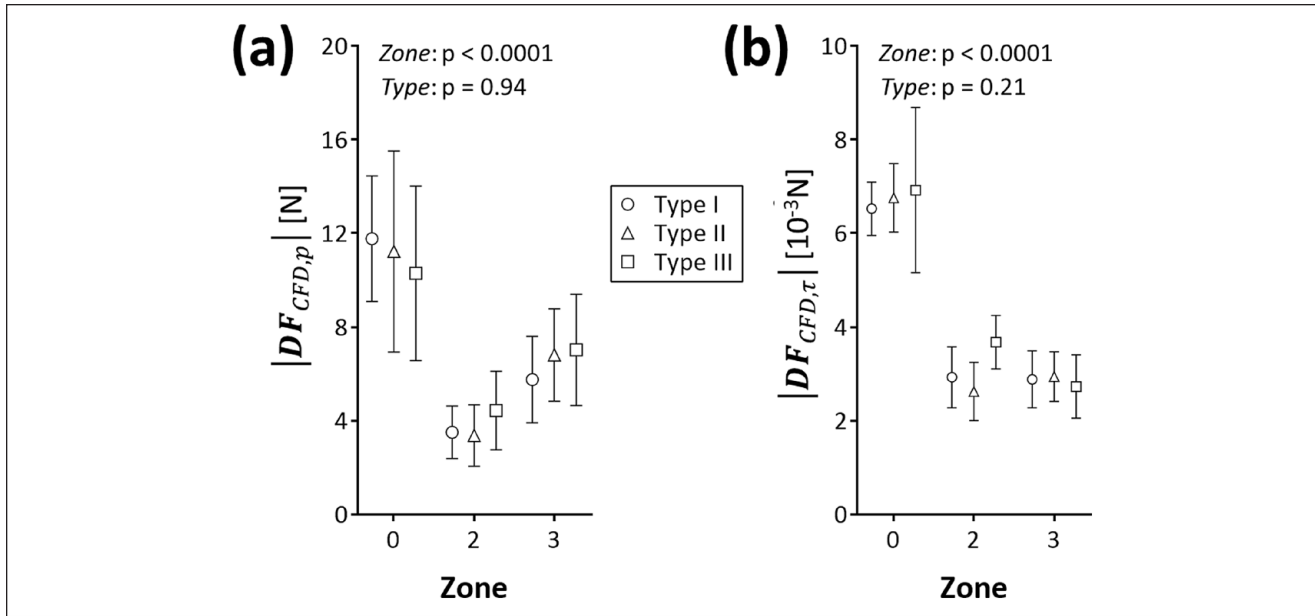


Figure 9. Repartition of displacement force magnitude between $|DF_{CFD,p}|$ and $|DF_{CFD,\tau}|$ according to (a) blood pressure and (b) wall shear stress contributions, respectively. CFD, computational fluid dynamics; DF, displacement force.

From a clinical standpoint, the fast-approximate analysis of CILCA arches confirms the presence of a force distribution over the proximal landing zones for TEVAR¹² that is preserved in different anatomies, reporting a much greater $|EST_{fast}|$ in zone 3 as compared with the adjacent zone 2. These features, along with previously described severe angulation and tortuosity of zone 3 in CILCA arch,¹⁹ confirm that zone 3 should be regarded as a biomechanically hostile landing zone for TEVAR in subjects with this anatomic configuration¹².

From a methodological standpoint, the proposed fast-approximate approach only requires patient-specific aortic geometry and a measure of central aortic pressure, both of which are available during TEVAR planning. The patient-specific anatomy can be accurately extracted from the computed tomography, which is already exploited because of its speed and ease of use to navigate and assess the patient-specific aortic anatomy,^{29,30} eg, through commercial and clinically oriented semi-automated platforms. Central aortic pressure is recorded in routine clinical practice and generally estimated using noninvasive methods,^{31,32} eg, through brachial cuff sphygmomanometer. In the present proof-of-concept, a physiological range of blood pressure was imposed and reproduced in the CFD analysis. To mimic the in vivo cuff measure of central blood pressure, this was estimated averaging the overall pressure distribution on the entire aortic arch wall. However, the fact that non-patient-specific pressures were used does not limit the main point of the present work: for a given pressure regime, the fast-approximate method we propose is a very good approximation of the more sophisticated and time-expensive CFD-based method.

From a conceptual standpoint, it is interesting to note that EST_{fast} , ie, the normalized version of DF_{fast} , can be expressed as the product of 2 factors each one accounting for the key features of the patient under examination: p and S .

The proportionality between EST_{fast} and S confirms our hypothesis on the key role of the patient-specific 3D anatomy in determining both entity and directions of DF_{fast} along the aortic arch. Specifically, we herein highlighted the peculiar biomechanical pattern of zone 3 in terms of the dimensionless shape vector S (Figure 4), whose magnitude, ie, $|S|$, is disproportionately increased with respect to the adjacent zone 2 in all the types of CILCA arch (Figure 4a). In addition, the upward dominating orientation of the S vector is remarkably exacerbated along the superior-inferior anatomical direction in zone 3, as revealed by the visibly low values of the γ direction cosine (Figure 4b). As preliminary tested on the small cohort of aneurysmatic anatomies with CILCA arch configuration (Figure 4c), the anterior orientation of S dominating in zone 3 well reflected the degree of aortic wall dilation, and the consequent altered orientation of DF_{fast} action on the aortic wall.

Hence, though further and more extensive validation is required, our data suggest that the dimensionless shape vector can effectively describe how pressure-driven blood forces are expected to act and impact on the thoracic aortic wall. This represents a valid biomechanical blueprint of the aortic arch morphology, which can be computed without measuring aortic pressure, and can be interpreted as a scaling factor of the aortic anatomic pattern, see equation (5). As exemplified in Figure 10, two main and complementary factors affecting the shape vector S can be highlighted in the aortic arch.

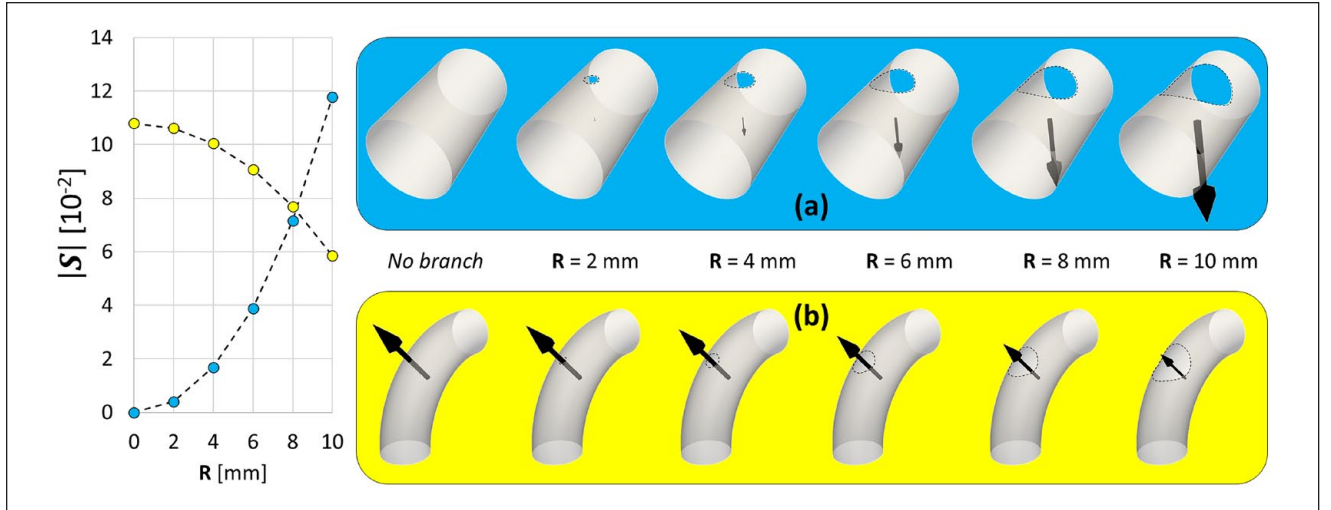


Figure 10. Impact of the dimension (ie, in terms of radius) of vessel branching on the computation of the shape vector S in a straight cylindrical surface (a) and in a curved pipe (b).

The first factor is determined by the presence of aortic branches and by the size of the respective origins: in a straight cylinder without branches S ideally has a zero magnitude, owing to the symmetry of the geometry (Figure 10a). In presence of a branch, at the origin cross section, the pressure within the branch is seen from the main vessel as a pressure load directed inwards; this effect is accounted for in equation (5) by flipping the normal n_i of the triangular faces within the branch origin. This effect causes an asymmetry and generates a non-zero S , whose magnitude increases as the extent of the branch origin increases.

The second factor, which can be superimposed to the former, is related to the curvature of the vessel: in a curved pipe (Figure 10b), for instance, S is generally oriented toward the outer curvature, ie, the convexity of the vessel. However, due to the presence of a branch on the convexity of the curved pipe, as in the case of the aortic arch, S progressively decreases in magnitude consistently with the compensatory action of the first geometrical factor.

Finally, the potential application of the fast-approximate approach may also pave the way for a novel and truly dynamic assessment of aortic DF . Current CFD analyses of aortic DFs ,^{6,7,10-12} though prescribing physiologically realistic volumetric flow rate and pressure waveforms, completely neglect the compliance of the aortic wall, which in reality undergoes cyclic deformation in response to pulsating blood pressure, and largely differs among various aortic diseases, such as aneurysm, dissections, and trauma. To overcome this limitation of CFD analyses, a fluid-structure interaction (FSI) model of the aortic arch should be implemented,^{33,34} but the time-expense of FSI simulations would be even greater than that of CFD analyses. Furthermore, the implementation of an FSI model would

pose several and relevant modeling issues, eg, the description of the patient-specific and heterogeneous aortic wall thickness and tissue mechanical properties.

In this respect, the proposed fast-approximate approach could be exploited, combining ECG-gated multiphase CT imaging,^{35,36} to reproduce the aortic arch geometry over the cardiac cycle, with the patient-specific monitoring of aortic pressure, eg, through continuous noninvasive arterial pressure measurements.³⁷ To this purpose, the process of aortic segmentation could be fastened by exploiting deep learning-based and fully automatic algorithms.³⁸⁻⁴⁰

Limitations

We recognize some limitations of our study.

First, whether the biomechanical environment of the bovine aortic arch variant can effectively entail an increased risk of postoperative complications after TEVAR still remains to be demonstrated. To this purpose, a multicenter ad hoc outcome study is currently in progress.

Second, we adopted the same flow boundary conditions in all the simulated cases, which, however, did not impact on the comparison of both DF_{fast} and EST_{fast} against CFD analysis in the different proximal landing zones of the aortic arch. Further efforts will be necessary to extend on a patient-specific basis the validation of the present fast-approximate approach. Comparisons will be made against more personalized CFD and FSI analysis including patient-specific boundary conditions, eg, obtainable from preoperative phase contrast magnetic resonance imaging (PC-MRI),²⁶ and exploiting commonly available clinical data.⁴¹

Third, we approximated the spatial blood pressure distribution within the aortic arch with a single, noninvasive and

clinically pertinent measure. Although only minor changes in blood pressure are expected along the aortic arch,^{14–16} the validity of this assumption should be further tested against *in vivo* evidence. This could be obtained either invasively or noninvasively: in the first case, measurements available in the cardiac catheterization laboratory,⁴² eg, in patients undergoing diagnostic catheterizations or percutaneous procedures, could be exploited. In the second case, the relative pressure field, and hence pressure space-dependency, within the aortic arch could be extracted from time-resolved velocity-encoded magnetic resonance imaging (4D Flow).^{43,44}

Conclusion

The present work provides a reliable and simplified method enabling a preoperative decision-making process for TEVAR through quantitative and physics-based parameters measured in aortic arch proximal landing zones, which allows further studies on the definition of clinically relevant threshold values of such parameters.

Declaration of Conflicting Interests

The author(s) declared no potential conflicts of interest with respect to the research, authorship, and/or publication of this article.


Funding

The author(s) disclosed receipt of the following financial support for the research, authorship, and/or publication of this article: The financial support of the Italian Ministry of Health (Ricerca Corrente and 5xmille) is gratefully acknowledged.

Ethics

The study was approved by the Ethics Committee of reference, i.e., Ethics Committee of IRCCS San Raffaele (Milan, Italy); protocol code “CardioRetro” number 122/int/2017 approved on September 14, 2017 and amended on July 18, 2019. Informed consent was waived by the Ethics Committee because of the retrospective nature of the study and the analysis of anonymized images. The study was conducted according to the principles outlined in the Declaration of Helsinki.

ORCID iDs

Francesco Sturla  <https://orcid.org/0000-0001-7317-304X>
Massimiliano M. Marrocco-Trischitta  <https://orcid.org/0000-0003-1707-9627>

Data Availability

Data and support material are available as part of the electronic Supplementary Material.

Supplementary Material

Supplemental material for this article is available online.

References

1. Grabenwöger M, Alfonso F, Bachet J, et al. Thoracic Endovascular Aortic Repair (TEVAR) for the treatment of aortic diseases: a position statement from the European Association for Cardio-Thoracic Surgery (EACTS) and the European Society of Cardiology (ESC), in collaboration with the European Association of Percutaneous Cardiovascular Interventions (EAPCI). *Eur J Cardiothorac Surg.* 2012;42:17–24.
2. Marrocco-Trischitta MM, Melissano G, Kahlberg A, et al. Chronic kidney disease classification stratifies mortality risk after elective stent graft repair of the thoracic aorta. *J Vasc Surg.* 2009;49(2):296–301.
3. Ranney DN, Yerokun BA, Benrashid E, et al. Outcomes of planned two-stage hybrid aortic repair with Dacron-replaced proximal landing zone. *Ann Thorac Surg.* 2018;106(4):1136–1142.
4. Böckler D, Brunkwall J, Taylor PR, et al. Thoracic endovascular aortic repair of aortic arch pathologies with the conformable thoracic aortic graft: early and 2 year results from a European Multicentre Registry. *Eur J Vasc Endovasc Surg.* 2016;51(6):791–800.
5. Marrocco-Trischitta MM, van Bakel TM, Romarowski RM, et al. The Modified Arch Landing Areas Nomenclature (MALAN) improves prediction of stent graft displacement forces: proof of concept by computational fluid dynamics modelling. *Eur J Vasc Endovasc Surg.* 2018;55(4):584–592.
6. Figueroa CA, Taylor CA, Chiou AJ, et al. Magnitude and direction of pulsatile displacement forces acting on thoracic aortic endografts. *J Endovasc Ther.* 2009;16(3):350–358.
7. Marrocco-Trischitta MM, Romarowski RM, de Beaufort HW, et al. The Modified Arch Landing Areas Nomenclature identifies hostile zones for endograft deployment: a confirmatory biomechanical study in patients treated by thoracic endovascular aortic repair. *Eur J Cardiothorac Surg.* 2019;55:990–997.
8. Marrocco-Trischitta MM, de Beaufort HW, Piffaretti G, et al. The Modified Arch Landing Areas Nomenclature predicts proximal endograft failure after thoracic endovascular aortic repair. *Eur J Cardiothorac Surg.* 2020;58:309–318.
9. Molony DS, Kavanagh EG, Madhavan P, et al. A computational study of the magnitude and direction of migration forces in patient-specific abdominal aortic aneurysm stent-grafts. *Eur J Vasc Endovasc Surg.* 2010;40(3):332–339.
10. Figueroa CA, Taylor CA, Yeh V, et al. Preliminary 3D computational analysis of the relationship between aortic displacement force and direction of endograft movement. *J Vasc Surg.* 2010;51(6):1488–1497; discussion 97.
11. Kandail H, Hamady M, Xu XY. Patient-specific analysis of displacement forces acting on fenestrated stent grafts for endovascular aneurysm repair. *J Biomech.* 2014;47:3546–3554.
12. Marrocco-Trischitta MM, Romarowski RM, Alaidroos M, et al. Computational fluid dynamics modeling of proximal landing zones for thoracic endovascular aortic repair in the bovine arch variant. *Ann Vasc Surg.* 2020;69:413–417.
13. Fung GS, Lam SK, Cheng SW, et al. On stent-graft models in thoracic aortic endovascular repair: a computational

- investigation of the hemodynamic factors. *Comput Biol Med.* 2008;38(4):484–489.
14. Luchsinger PC, Snell RE, Patel DJ, Fry DL. Instantaneous pressure distribution along the human aorta. *Circ Res.* 1964;15:503–510.
 15. Alastruey J, Hunt AA, Weinberg PD. Novel wave intensity analysis of arterial pulse wave propagation accounting for peripheral reflections. *Int J Numer Method Biomed Eng.* 2014;30(2):249–279.
 16. Charlton PH, Mariscal Harana J, Vennin S, et al. Modeling arterial pulse waves in healthy aging: a database for in silico evaluation of hemodynamics and pulse wave indexes. *Am J Physiol Heart Circ Physiol.* 2019;317:H1062–H1085.
 17. Popieluszko P, Henry BM, Sanna B, et al. A systematic review and meta-analysis of variations in branching patterns of the adult aortic arch. *J Vasc Surg.* 2018;68(1):298–306.
 18. Rylski B, Pacini D, Beyersdorf F, et al. Standards of reporting in open and endovascular aortic surgery (STORAGE guidelines). *Eur J Cardiothorac Surg.* 2019;56:10–20.
 19. Marrocco-Trischitta MM, Alaidroos M, Romarowski RM, et al. Geometric pattern of proximal landing zones for thoracic endovascular aortic repair in the bovine arch variant. *Eur J Vasc Endovasc Surg.* 2020;59(5):808–816.
 20. Marrocco-Trischitta MM, Alaidroos M, Romarowski RM, et al. Aortic arch variant with a common origin of the innominate and left carotid artery as a determinant of thoracic aortic disease: a systematic review and meta-analysis. *Eur J Cardiothorac Surg.* 2020;57:422–427.
 21. Marrocco-Trischitta MM, de Beaufort HW, Secchi F, et al. A geometric reappraisal of proximal landing zones for thoracic endovascular aortic repair according to aortic arch types. *J Vasc Surg.* 2017;65(6):1584–1590.
 22. Madhwal S, Rajagopal V, Bhatt DL, et al. Predictors of difficult carotid stenting as determined by aortic arch angiography. *J Invasive Cardiol.* 2008;20(5):200–204.
 23. Morbiducci U, Ponzini R, Rizzo G, et al. In vivo quantification of helical blood flow in human aorta by time-resolved three-dimensional cine phase contrast magnetic resonance imaging. *Ann Biomed Eng.* 2009;37(3):516–531.
 24. Gallo D, De Santis G, Negri F, et al. On the use of in vivo measured flow rates as boundary conditions for image-based hemodynamic models of the human aorta: implications for indicators of abnormal flow. *Ann Biomed Eng.* 2012;40(3):729–741.
 25. Antiga L, Piccinelli M, Botti L, et al. An image-based modeling framework for patient-specific computational hemodynamics. *Med Biol Eng Comput.* 2008;46(11):1097–1112.
 26. Romarowski RM, Lefieux A, Morganti S, et al. Patient-specific CFD modelling in the thoracic aorta with PC-MRI-based boundary conditions: a least-square three-element Windkessel approach. *Int J Numer Method Biomed Eng.* 2018;34(11):e3134.
 27. Williams B, Mancia G, Spiering W, et al. [2018 ESC/ESH Guidelines for the management of arterial hypertension. The Task Force for the management of arterial hypertension of the European Society of Cardiology (ESC) and the European Society of Hypertension (ESH)]. *Giornale Italiano Di Cardiologia (2006).* 2018;19:3s–73s.
 28. Tasso P, Lodi Rizzini M, Raptis A, et al. In-stent graft helical flow intensity reduces the risk of migration after endovascular aortic repair. *J Biomech.* 2019;94:170–179.
 29. Upchurch Jr GR, Escobar GA, Azizzadeh A, et al. Society for Vascular Surgery clinical practice guidelines of thoracic endovascular aortic repair for descending thoracic aortic aneurysms. *J Vasc Surg.* 2021;73:55S–83S.
 30. Pua U, Tay KH, Tan BS, et al. CT appearance of complications related to thoracic endovascular aortic repair (TEVAR): a pictorial essay. *Eur Radiol.* 2009;19(5):1062–1068.
 31. Muntner P, Einhorn PT, Cushman WC, et al. Blood pressure assessment in adults in clinical practice and clinic-based research: JACC scientific expert panel. *J Am Coll Cardiol.* 2019;73:317–335.
 32. McEniery CM, Cockcroft JR, Roman MJ, et al. Central blood pressure: current evidence and clinical importance. *Eur Heart J.* 2014;35(26):1719–1725.
 33. Savabi R, Nabaei M, Farajollahi S, et al. Fluid structure interaction modeling of aortic arch and carotid bifurcation as the location of baroreceptors. *Int J Mech Sci.* 2020;165:105222.
 34. Pons R, Guala A, Rodríguez-Palomares JF, et al. Fluid-structure interaction simulations outperform computational fluid dynamics in the description of thoracic aorta haemodynamics and in the differentiation of progressive dilation in Marfan syndrome patients. *R Soc Open Sci.* 2020;7(2):191752.
 35. Baliga RR, Nienaber CA, Bossone E, et al. The role of imaging in aortic dissection and related syndromes. *JACC Cardiovasc Imaging.* 2014;7(4):406–424.
 36. Yanagaki S, Ueda T, Masuda A, et al. Detection of the intimal tear in aortic dissection and ulcer-like projection in intramural hematoma: usefulness of full-phase retrospective ECG-gated CT angiography. *Jpn J Radiol.* 2020;38(11):1036–1045.
 37. Wagner JY, Negulescu I, Schöfthaler M, et al. Continuous noninvasive arterial pressure measurement using the volume clamp method: an evaluation of the CNAP device in intensive care unit patients. *J Clin Monit Comput.* 2015;29(6):807–813.
 38. Cao L, Shi R, Ge Y, et al. Fully automatic segmentation of type B aortic dissection from CTA images enabled by deep learning. *Eur J Radiol.* 2019;121:108713.
 39. Fantazzini A, Esposito M, Finotello A, et al. 3D Automatic segmentation of aortic computed tomography angiography combining multi-view 2D convolutional neural networks. *Cardiovasc Eng Technol.* 2020;11(5):576–586.
 40. Isensee F, Jaeger PF, Kohl SAA, et al. NnU-Net: a self-configuring method for deep learning-based biomedical image segmentation. *Nat Methods.* 2021;18(2):203–211.
 41. Bonfanti M, Franzetti G, Maritati G, et al. Patient-specific haemodynamic simulations of complex aortic dissections informed by commonly available clinical datasets. *Med Eng Phys.* 2019;71:45–55.
 42. Nishimura RA, Carabello BA. Hemodynamics in the cardiac catheterization laboratory of the 21st century. *Circulation.* 2012;125:2138–2150.
 43. Bouaou K, Bargiotas I, Diertenbeck T, et al. Analysis of aortic pressure fields from 4D flow MRI in healthy volunteers: associations with age and left ventricular remodeling. *J Magn Reson Imaging.* 2019;50(3):982–993.
 44. Saitta S, Pirola S, Piatti F, et al. Evaluation of 4D flow MRI-based non-invasive pressure assessment in aortic coarctations. *J Biomech.* 2019;94:13–21.